




Cite this: *Sustainable Energy Fuels*,  
2023, 7, 4618

# Unravelling the role of iron carbide in oxygen reduction catalysts for rechargeable zinc–air batteries: a comprehensive kinetics & mechanistic study†

S. Arya Gopal, Anook Nazer Eledath and Azhagumuthu Muthukrishnan \*

Rechargeable metal–air batteries are an emerging electrochemical energy storage technology wherein the invention of bifunctional electrocatalysts for the oxygen reduction reaction (ORR) and oxygen evolution reaction (OER) plays a critical role in the device's performance. Recently, Fe<sub>3</sub>C-based carbon materials have been reported for their excellent bifunctional activity. The lack of understanding in defining the role of Fe<sub>3</sub>C impedes the design of high-performance catalysts. Fe<sub>3</sub>C on carbon (Fe<sub>3</sub>C/C) and Fe<sub>3</sub>C on nitrogen-doped carbon (Fe<sub>3</sub>C/NC) are synthesised using various carbon substrates. The mechanistic analysis from the rotating ring-disk electrode voltammogram demonstrates the formation of 4-electron active sites while introducing Fe<sub>3</sub>C and nitrogen in the graphitic carbon substrate, and the reason for the superior ORR activity is discussed. The activity and stability are evaluated using a zinc–air battery experiment. Fe<sub>3</sub>C & N-doped Vulcan carbon exhibits higher power density (167 mW cm<sup>−2</sup>) and specific capacity (756 mA h g<sub>Zn</sub><sup>−1</sup> @ 20 mA cm<sup>−2</sup>). Besides, Fe<sub>3</sub>C & N-doped Vulcan carbon shows excellent stability with 88% efficiency after 300 cycles (20 minutes per cycle) of continuous charge–discharge operation at a current density of 5 mA cm<sup>−2</sup>. All the Fe<sub>3</sub>C/NC catalysts show excellent stability in the OER region, and this study guides the futuristic design of Fe<sub>3</sub>C-based catalysts for zinc–air battery electrodes.

Received 22nd May 2023  
Accepted 7th August 2023

DOI: 10.1039/d3se00676j

rsc.li/sustainable-energy

## 1. Introduction

Developing platinum-free electrocatalysts for the oxygen reduction reaction (ORR) at cathodes of fuel cells and metal–air batteries is one of the paramount research studies in energy conversion and storage systems. Among the non-platinum group metal catalysts developed so far, Fe-containing N-doped carbon (Fe–N/C) materials are promising potential alternatives for state-of-the-art catalysts in terms of activity and durability. The activity of Fe–N/C can be tuned in many ways, such as by using suitable precursors, pyrolysis temperature, time, atmosphere, *etc.* The real active sites of Fe–N/C catalysts remain unsolved despite various theories proposed depicting different active sites for O<sub>2</sub> adsorption.<sup>1–12</sup> Though the Fe content is very low (traces to 3 wt%) in most of the Fe–N/C catalysts, it was believed that Fe–N<sub>x</sub> active sites are responsible for the superior ORR activity. Besides Fe–N<sub>x</sub>, multitudinous iron-containing compounds were found in Fe–N/C catalysts, such as oxides, carbides, encapsulated iron nanoparticles, *etc.* It is essential to

study the role of individual components in Fe–N/C catalysts to understand real active sites, which helps in designing very active and highly durable electrocatalysts for the ORR.

Iron carbides are the frequently encountered species in heat-treated Fe–N/C catalysts. It is well-known that heating carbon with iron precursors at higher temperatures (>700 °C) generates iron carbides.<sup>13–16</sup> Hence the formation of iron carbide is inevitable in the process of Fe–N/C synthesis *via* the pyrolysis of organic precursors in an inert atmosphere. The synthesis of Fe<sub>3</sub>C from various precursors and their ORR activity were reported elsewhere.<sup>15,17–26</sup> Nevertheless, most reported materials were synthesised from Fe and nitrogen-containing precursors and denoted as Fe<sub>3</sub>C@N–C, Fe@Fe<sub>3</sub>C/Fe–N<sub>x</sub>, Fe<sub>3</sub>C/Fe–N<sub>x</sub>, *etc.* In these catalysts, the origin of the ORR activity is not only from the Fe<sub>3</sub>C sites but also from the Fe–N<sub>x</sub> and N–C active sites formed during the process. The ORR activity and mechanism of Fe<sub>3</sub>C (without nitrogen precursors) on carbon supports were not analysed in the literature. The role of Fe<sub>3</sub>C can be demonstrated only in the absence of any other heteroatoms, particularly the absence of Fe–N<sub>x</sub> active sites.

Fe<sub>3</sub>C/Fe–N<sub>x</sub> or Fe–Fe<sub>3</sub>C encapsulated N-doped carbon materials were studied, and their improved ORR activity was observed in the literature. The reason for the improved activity was explained by the synergistic effect of the encapsulated Fe<sub>3</sub>C

School of Chemistry, Indian Institute of Science Education Research Thiruvananthapuram, Maruthamala P.O., Vithura 695 551, Kerala, India. E-mail: muthukrishnan@iisertvm.ac.in

† Electronic supplementary information (ESI) available. See DOI: <https://doi.org/10.1039/d3se00676j>



with Fe–N<sub>x</sub> or N–C active sites.<sup>14,27–33</sup> In the case of Fe<sub>3</sub>C/Fe–N<sub>x</sub> composites, the relative content of each species determines the mechanistic pathway. Fe–N<sub>x</sub> promotes the 4e<sup>−</sup> direct pathway whereas Fe<sub>3</sub>C directs the reduction *via* the stepwise pathway (2 + 2e<sup>−</sup> ORR).<sup>34,35</sup> The N-doped carbon encapsulated Fe<sub>3</sub>C nanoparticles are active towards the oxygen evolution reaction (OER), whereas Fe–N<sub>x</sub> or N–C active sites are known for the ORR. Hence the dual active sites of Fe<sub>3</sub>C/Fe–N<sub>x</sub> composites act as a bifunctional catalyst in Zn–air batteries.<sup>19,30,36,37</sup> It was also believed that the formation of Fe<sub>3</sub>C suppresses the formation of Fe–N<sub>x</sub> active sites, which is mandatory for the ORR. Thus, the formation of Fe<sub>3</sub>C (2-electron active sites) was suppressed by adding sulphur, which enhanced Fe–N<sub>x</sub> sites.<sup>38</sup> The theoretical analysis indicates that Fe<sub>3</sub>C enhances the ORR activity by minimising the adsorption activation energy. However, the ORR kinetics limited by the strongly adsorbed intermediates, especially the reductive desorption of \*OH from the active sites, is not thermodynamically favoured.<sup>13</sup>

Herein, the role of Fe<sub>3</sub>C present in heat-treated Fe–N/C catalysts is demonstrated using pure Fe<sub>3</sub>C on various carbon supports with different porosities. The encapsulated or Fe<sub>3</sub>C-supported carbon materials are studied using RRDE voltammetry, and their role in the ORR is defined by analysing the mechanism using kinetic parameters. The Fe<sub>3</sub>C encapsulated or Fe<sub>3</sub>C supported by N-doped carbon materials is also studied to understand the role of each active site (Fe<sub>3</sub>C, Fe–N and N–C) towards the ORR. The zinc–air battery testing demonstrates excellent OER performance for longer cycles, revealing the dual active site concepts for the OER and ORR in Fe<sub>3</sub>C-containing N-doped carbon catalysts. The role of carbon supports is also discussed elaborately.

## 2. Methodology

### 2.1 Synthesis of Fe<sub>3</sub>C/C and Fe<sub>3</sub>C/NC composites

The synthesis of Fe<sub>3</sub>C on carbon materials was explained as shown in Fig. 1. Briefly, the conductive carbon (Ketjen black EC300J (KB) or Vulcan carbon XC-72 (VC) or graphene oxide (GO)) was uniformly dispersed in 0.1 M Fe(NO<sub>3</sub>)<sub>3</sub>·9H<sub>2</sub>O

solution, followed by the slow addition of 0.05 M K<sub>4</sub>(Fe(CN)<sub>6</sub>) to form a carbon–Prussian blue (PB) composite. The precipitate was washed with DI water and dried. The carbon–PB composite was transferred into an alumina boat and kept in a tube furnace. The furnace was heated at a rate of 5 °C min<sup>−1</sup> under a flow of N<sub>2</sub> (flow rate: 40 mL min<sup>−1</sup>) and was kept at 900 °C for 2 hours before cooling to room temperature naturally. Finally, the samples were collected from the furnace and washed with 0.1 M HCl to remove excess iron species from the material. Thus the synthesised material is referred to as Fe<sub>3</sub>C/C (C refers to KB or VC or rGO). The heat-treated (900 °C) bare carbon substrates (synthesised using a similar method adopted for Fe<sub>3</sub>C/C) were employed as control samples to study the role of Fe<sub>3</sub>C. Previously, the carbon samples (KB and VC) were washed with 1 M HCl solution to remove metal impurities, whereas GO was synthesized using a modified Hummers' method, as reported earlier.<sup>39</sup>

The Fe<sub>3</sub>C/NC materials were synthesised from a mixture of previously synthesised Fe<sub>3</sub>C/C and dicyandiamide (DCDA) in a ratio of 1 : 10. The mixture was transferred to an alumina boat and heated at 700 °C with a ramp rate of 3 °C min<sup>−1</sup> (other conditions are very similar to those in the procedure described above). Thus the synthesised material is referred to as N-doped Fe<sub>3</sub>C/carbon (Fe<sub>3</sub>C/NC) catalysts.

Pure Fe<sub>3</sub>C was synthesized by the thermal decomposition of Prussian blue (PB) at higher temperatures. An aqueous solution of 0.1 M Fe(NO<sub>3</sub>)<sub>3</sub>·9H<sub>2</sub>O was mixed with 0.05 M K<sub>4</sub>(Fe(CN)<sub>6</sub>) with constant stirring, producing a blue colour precipitate of PB. The PB was filtered and washed with ethanol and water. The vacuum-dried PB was heated to 900 °C under similar conditions described above to get Fe<sub>3</sub>C. The formation of pure Fe<sub>3</sub>C was further confirmed by X-ray diffraction spectroscopy.

### 2.2 Electrochemistry

The electrochemical studies were performed using a PARSTAT multichannel potentiostat in a custom-made electrochemical cell (200 ml). The linear sweep hydrodynamic voltammetric technique was employed using a rotating ring-disk electrode (RRDE, PINE Instruments) in O<sub>2</sub>-saturated 0.1 M KOH electrolyte. The RRDE consists of a glassy carbon (GC) disk (5.6 mm diameter) and a Pt ring electrode with a theoretical collection efficiency of 0.37. The GC disk of the RRDE was modified with the catalysts as given below. The catalytic ink was prepared by weighing 5 mg of the catalysts (Fe<sub>3</sub>C or Fe<sub>3</sub>C/C or Fe<sub>3</sub>C/NC or N–C) with isopropanol (0.15 ml), Type 1 water (0.15 ml) and a Nafion® (0.05 ml of 5 wt%) binder.<sup>40,41</sup> The catalyst ink was made by dispersing the above mixture using a sonicator. A known amount of the ink was taken using a micropipette and drop-coated on the GC disk of the RRDE, maintaining a loading density of 200 µg cm<sup>−2</sup>. The catalyst-modified GC disk, carbon cloth with a graphite rod and Ag/AgCl (sat. KCl) were used as working, counter and reference electrodes, respectively. All the potentials were corrected against a reversible hydrogen electrode (RHE) using the pH of the electrolyte. Blank experiments in N<sub>2</sub>-saturated electrolytes were performed to measure the background charging current. The disk electrode was scanned

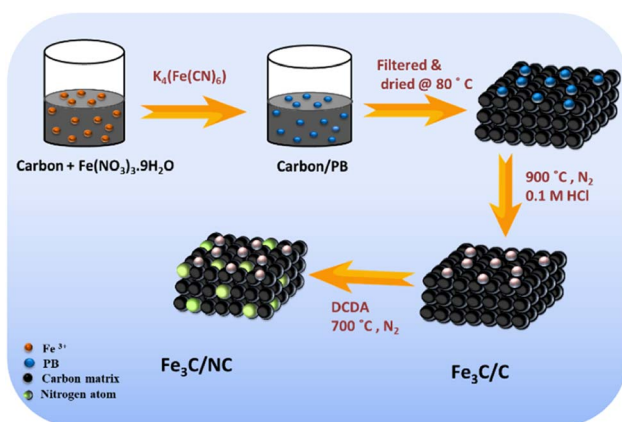


Fig. 1 Schematic representation of the synthetic methods of Fe<sub>3</sub>C/C and Fe<sub>3</sub>C/NC materials.



linearly from 1 V to 0 V at a scan rate of  $10 \text{ mV s}^{-1}$ , whereas the ring electrode was kept at a constant potential of 1.2 V to estimate the  $\text{H}_2\text{O}_2$  intermediate quantitatively. The stability of the catalysts was analysed using the accelerated durability test.<sup>42</sup> Briefly, the catalyst-coated GC rotating disk electrode (5 mm diameter) was scanned between 1.0 and 0.6 V at a scan rate of  $100 \text{ mV s}^{-1}$  for 10 000 cycles in an  $\text{O}_2$ -saturated 0.1 M KOH electrolyte. Linear sweep voltammetry before and after the durability cycles was performed at 1600 rpm rotational speed in  $\text{O}_2$ -saturated 0.1 M KOH electrolyte (scan rate is  $10 \text{ mV s}^{-1}$ ).

### 3. Results and discussion

#### 3.1 Characterisation

X-ray diffraction (XRD) spectroscopy (Bruker XRD,  $\text{CuK}\alpha$ ,  $\lambda = 1.5406 \text{ \AA}$ , 40 kV, 40 mA) was used to confirm the crystalline nature of the materials ( $\text{Fe}_3\text{C}$  and carbon). The diffraction patterns of pure  $\text{Fe}_3\text{C}$  nanoparticles (JCPDS No. 35-0772) have been compared with those of the synthesised composites.<sup>20</sup> All the synthesised materials (before the acid-washing step) show a characteristic peak at  $45^\circ$ , which corresponds to the bulk Fe

particles (JCPDS-06-0696) formed along with the  $\text{Fe}_3\text{C}$  nanoparticles (Fig. S1†).<sup>26</sup> The acid-washed  $\text{Fe}_3\text{C}/\text{C}$  compounds exhibit a diffraction peak at  $25.5^\circ$  (002), which corresponds to the graphitic carbon. Only excess  $\text{Fe}_3\text{C}$  is removed during acid-washing, and the presence of  $\text{Fe}_3\text{C}$  is confirmed by the less intense peaks (Fig. 2a). The encapsulated  $\text{Fe}_3\text{C}$  or Fe nanoparticles present inside the micro and mesopores of the carbon matrix remain in the materials after acid washing. In the case of  $\text{Fe}_3\text{C}/\text{NrGO}$ , a small peak observed at  $35^\circ$  indicates the presence of iron oxides ( $\text{Fe}_2\text{O}_3$ ), and later, it was confirmed by elemental mapping using transmission electron microscopy (TEM).

The quantitative estimation of Fe in  $\text{Fe}_3\text{C}$  or  $\text{Fe}_3\text{C}/\text{NC}$  was performed using the thermogravimetric analysis<sup>43</sup> (SDT-Q-600, TA Instruments). More accurate measurements using inductively coupled plasma optical emission spectroscopy (ICP-OES) result in a significant error due to the difficulty in sample preparation for ICP-OES (incomplete extraction of metal species using acids). The TGA experiment was performed under a flow of air. From the thermogravimetric curves, the weight loss observed above  $450^\circ\text{C}$  (Fig. 2b) can be attributed to the oxidation of carbonaceous content. The TGA curves are parallel to the

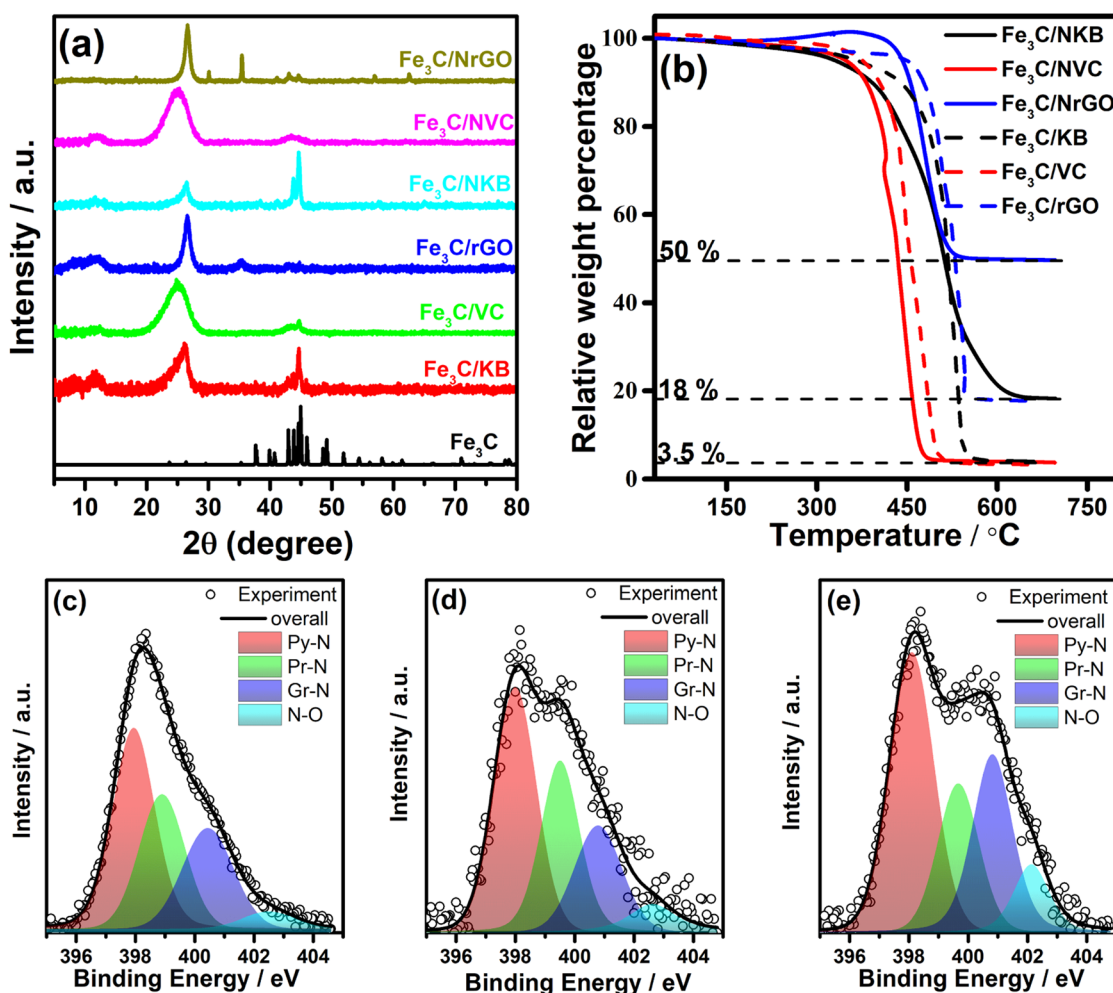


Fig. 2 (a) The powder XRD pattern of  $\text{Fe}_3\text{C}$ ,  $\text{Fe}_3\text{C}/\text{C}$  and  $\text{Fe}_3\text{C}/\text{NC}$  composites. (b) TGA plots of  $\text{Fe}_3\text{C}/\text{C}$  and  $\text{Fe}_3\text{C}/\text{NC}$  composites to estimate the iron contents in the samples. N 1s XPS spectra of (c)  $\text{Fe}_3\text{C}/\text{NKB}$ , (d)  $\text{Fe}_3\text{C}/\text{NVC}$  and (e)  $\text{Fe}_3\text{C}/\text{NrGO}$  compounds and their components after deconvolution.



x-axis beyond 650 °C, indicating that all the carbon-based materials are burned out and the remaining must be the oxides of iron species. The powder XRD analysis reveals the formation of  $\text{Fe}_2\text{O}_3$  after the removal of carbon content (Fig. S2†). The Fe content was calculated from  $\text{Fe}_2\text{O}_3$ , as shown in Table S1.† The higher Fe content in  $\text{Fe}_3\text{C}/\text{rGO}$  can be explained by the relatively significant carbon content loss of the carbon support (GO) compared with other carbon supports. The Fe content of  $\text{Fe}_3\text{C}/\text{NVC}$  retains its original values, whereas the Fe in  $\text{Fe}_3\text{C}/\text{NKB}$  and  $\text{Fe}_3\text{C}/\text{NrGO}$  increased to 3 times that of the Fe content in  $\text{Fe}_3\text{C}/\text{C}$ . This indicates that KB and rGO lose carbon content during the N-doping.

X-ray photoelectron spectroscopy (XPS) exhibits the elements in the materials and their chemical states. XPS experiments (Omicron Nanotech, excitation source:  $\text{MgK}\alpha$ , kinetic energy: 1253.6 eV in constant analyser energy mode with a pass energy of 50 eV) were performed to investigate the bonding nature of the elements. The survey spectra of  $\text{Fe}_3\text{C}/\text{C}$  compounds indicate that the major component of the materials consists of carbon (Fig. S3†), wherein the C-1s peak was centred at 284.2 eV, corresponding to  $\text{sp}^2$  carbon. The small pre-peak at 283.4 eV represents the carbon bonded with Fe (in  $\text{Fe}_3\text{C}$ ). The deconvoluted peak from 286 to 288 eV indicates the carboxyl group (Fig. S4†). Fe is not seen in the survey spectra because of the carbon layers encapsulating  $\text{Fe}_3\text{C}$ , which makes it more difficult to detect the core  $\text{Fe}_3\text{C}$ . However,  $\text{Fe}_3\text{C}/\text{NKB}$  and  $\text{Fe}_3\text{C}/\text{NrGO}$  show less intense peaks at 708.6 eV ( $2\text{p}_{3/2}$ ) and 721.7 eV ( $2\text{p}_{1/2}$ ), corresponding to the Fe-2p XPS peaks (Fig. S5†). No Fe-2p peak was observed due to the lower Fe content in  $\text{Fe}_3\text{C}/\text{NVC}$ . Fig. 2c–e show the N-1s XPS spectra of  $\text{Fe}_3\text{C}/\text{NC}$  compounds, which were deconvoluted into four peaks corresponding to pyridinic, pyrrolic, and graphitic nitrogen and nitrogen oxides. The nitrogen content estimated from the XPS peaks is given in Table S1.† Due to the lower Fe content in  $\text{Fe}_3\text{C}/\text{NVC}$ , nitrogen doping is significantly reduced to 1.2 wt%. The majority of the nitrogen content is in the form of pyridinic nitrogen, known for its positive impact on the ORR activity.<sup>7,44,45</sup>

The surface area and pore size distribution were measured using  $\text{N}_2$ -sorption isotherms (Micrometrics 3Flex analyser), as shown in Fig. 3. The  $\text{Fe}_3\text{C}/\text{C}$  and  $\text{Fe}_3\text{C}/\text{NC}$  materials exhibit type

IV adsorption isotherms with H3/H4 hysteresis loops. The Brunauer–Emmett–Teller (BET) surface area and the pore volume of the composite materials are listed in Table 1. Pure KB exhibits the highest surface area, followed by rGO and VC. BET surface area of the composites ( $\text{Fe}_3\text{C}/\text{C}$ ) is smaller than the corresponding bare carbon support surface area, and it can be rationalised by filling pores (of the carbon support) with non-porous  $\text{Fe}_3\text{C}$ . The  $\text{Fe}_3\text{C}/\text{C}$  compounds before acid washing ( $\text{Fe}_3\text{C}/\text{C}(\text{BAW})$ ) show less surface area than  $\text{Fe}_3\text{C}/\text{C}$  (Fig. S6†), supporting the above statement. The substantial decrease in the surface area of  $\text{Fe}_3\text{C}/\text{NC}$  compared with  $\text{Fe}_3\text{C}/\text{C}$  can be explained as follows. A graphitic carbon layer was formed on the surface of porous carbon materials during the pyrolysis at a higher temperature. The subsequent reduction in the pore volume from bare carbon to  $\text{Fe}_3\text{C}/\text{C}$  to  $\text{Fe}_3\text{C}/\text{NC}$  validates the pore blocking by  $\text{Fe}_3\text{C}$  followed by the graphitisation. The non-linear density functional theory (NLDFT) modelling of pore size (Fig. S7†) indicates no significant changes in the pore size distribution of  $\text{Fe}_3\text{C}/\text{KB}$  and  $\text{Fe}_3\text{C}/\text{VC}$  from their corresponding carbon supports. However, rGO lost its micropores after the incorporation of  $\text{Fe}_3\text{C}$  followed by the N-doping. The pore size distribution curves of  $\text{Fe}_3\text{C}/\text{NC}$  show a decrease in micropores with the formation of meso and macropores. The decrease in the surface area in each step (carbon to  $\text{Fe}_3\text{C}/\text{C}$  to  $\text{Fe}_3\text{C}/\text{NC}$ ) is less pronounced in VC composites<sup>46</sup> due to the low Fe content (corroborated by TGA analysis).

The morphology of the  $\text{Fe}_3\text{C}/\text{C}$  composites was analysed using high-resolution TEM images which demonstrate the presence of  $\text{Fe}_3\text{C}$  particles distributed on the carbon support (Fig. 4). The  $\text{Fe}_3\text{C}$  nanoparticles are encapsulated by the graphite layer (Fig. S9†), and  $\text{Fe}_3\text{C}$  particles were seen to be less than 50 nm in size. However,  $\text{Fe}_3\text{C}$  formed on rGO is larger in size as bulky particles. The selected area diffraction (SAED) pattern of  $\text{Fe}_3\text{C}/\text{C}$  indicates fringes with a  $d$ -spacing value of 0.24 and 0.2, corresponding to the 112 and 121 planes of  $\text{Fe}_3\text{C}$ .<sup>29,47</sup> The TEM images of  $\text{Fe}_3\text{C}/\text{NC}$  compounds indicate the presence of connected carbon particles with occasional nanotubes in  $\text{Fe}_3\text{C}/\text{NKB}$ , and more pictures are shown in Fig. S10.† The high-angle annular dark-field scanning transmission electron microscopic (HAADF-STEM) images clearly distinguish the

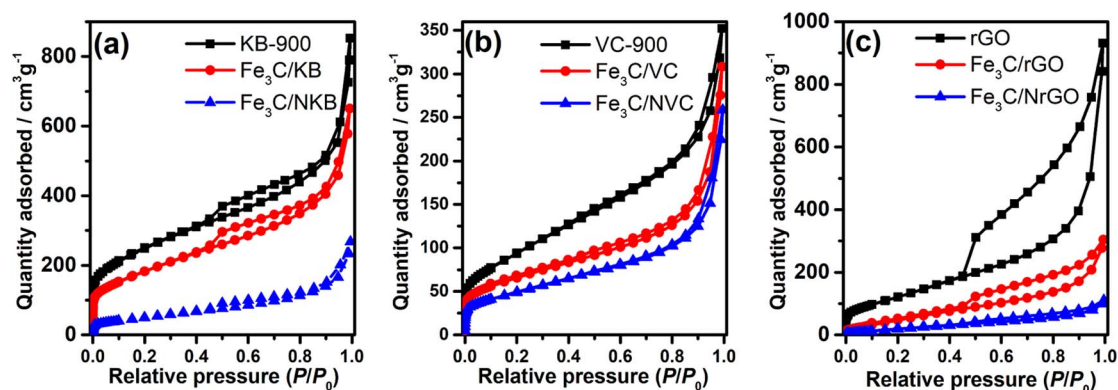


Fig. 3 The  $\text{N}_2$ -sorption isotherms of carbon supports (a) KB, (b) VC and (c) rGO before and after the incorporation of  $\text{Fe}_3\text{C}$  and  $\text{Fe}_3\text{C}$  followed by N-doping.





Table 1 Parameters obtained from the N<sub>2</sub>-adsorption isotherm

Compound	$S_{\text{total}}$ (m <sup>2</sup> g <sup>-1</sup> )	$S_{\text{micro}}^a$ (m <sup>2</sup> g <sup>-1</sup> )	$S_{\text{meso}}^b$ (m <sup>2</sup> g <sup>-1</sup> )	$V_{\text{total}}^c$ (cm <sup>3</sup> g <sup>-1</sup> )	$V_{\text{micro}}^d$ (cm <sup>3</sup> g <sup>-1</sup> )	$V_{\text{meso}}^e$ (cm <sup>3</sup> g <sup>-1</sup> )
KB-900	891	71.4	309.3	1.320	0.025	0.223
Fe <sub>3</sub> C/KB	654	55.7	278.8	1.007	0.019	0.20
Fe <sub>3</sub> C/NKB	155	—	107.6	0.416	—	0.080
VC-900	335	35.0	138.6	0.545	0.010	0.109
Fe <sub>3</sub> C/VC	235	15.7	82.8	0.447	0.008	0.05
Fe <sub>3</sub> C/NVC	157	—	71.2	0.400	—	0.058
rGO	430	6.2	489.4	1.442	0.012	0.450
Fe <sub>3</sub> C/rGO	176	3.4	207.9	0.471	0.003	0.150
Fe <sub>3</sub> C/NrGO	88	—	70.7	0.171	—	0.054

<sup>a</sup> Microporous surface area ( $S_{\text{mic}}$ ). <sup>b</sup> Mesoporous surface area ( $S_{\text{meso}}$ ) obtained from Barrett-Joyner-Halenda (BJH) method. <sup>c</sup> Total pore volume.

<sup>d</sup> Microporous volume ( $V_{\text{mic}}$ ) obtained from the  $t$ -plot. <sup>e</sup> Mesoporous volume ( $V_{\text{meso}}$ ).

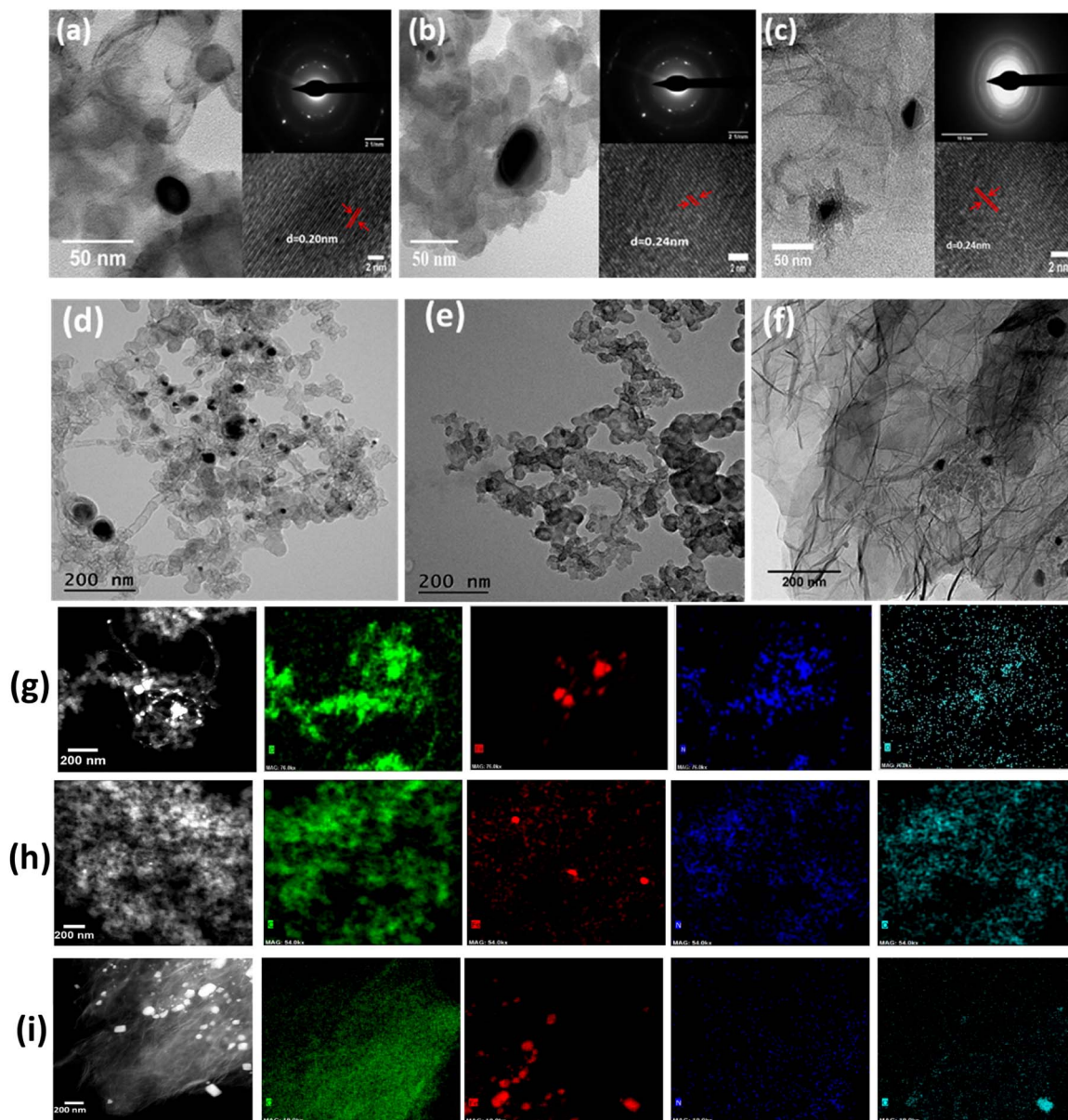


Fig. 4 High-resolution TEM images of Fe<sub>3</sub>C/C (a–c) and Fe<sub>3</sub>C/NC (d–f). From left to right: KB, VC and rGO supported Fe<sub>3</sub>C with and without N-doped carbon. HAADF-STEM images and EELS elemental mapping of (g) Fe<sub>3</sub>C/NKB, (h) Fe<sub>3</sub>C/NVC, and (i) Fe<sub>3</sub>C/NrGO. From left to right: HAADF-STEM images and carbon, iron, nitrogen and oxygen elemental mapping.



individual  $\text{Fe}_3\text{C}$  particles. The electron energy loss spectroscopy (EELS) elemental mapping confirms the presence of carbon, iron, nitrogen and oxygen distributed in the materials. Besides  $\text{Fe}_3\text{C}$ , the  $\text{Fe}_2\text{O}_3$  formation is also confirmed based on overlapping the individual elemental mappings in the composites. However, other than  $\text{Fe}_3\text{C}/\text{NrGO}$ , the XRD cannot show any  $\text{Fe}_2\text{O}_3$  peaks, as reported earlier.

### 3.2. Oxygen reduction reaction activity

Fig. 5a–c show RRDE voltammograms of the ORR on bare carbon,  $\text{Fe}_3\text{C}/\text{C}$  and  $\text{Fe}_3\text{C}/\text{NC}$  catalysts. The onset ( $E_{\text{onset}}$ ) potential (kinetically controlled region), half-wave ( $E_{1/2}$ ) potential (mixed kinetic-diffusion controlled region) and limiting current density ( $j_{\text{DL}}$ ) (diffusion controlled region) are used as activity descriptors to compare the ORR activity (Table S4†). The bare carbon materials show a typical double sigmoidal curve, pertaining to the 2-electron ORR ( $\text{O}_2$  to  $\text{H}_2\text{O}_2$ ) at lower overpotentials ( $>0.4$  V) and 2 + 2-electron ORR ( $\text{O}_2$  to  $\text{H}_2\text{O}$  via  $\text{H}_2\text{O}_2$ ) at higher overpotentials ( $<0.4$  V). The number of electrons ( $n$ ) is estimated using ring and disk currents (see the ESI†), which is close to 2, corroborating the 2-electron ORR. However, it is increasing to 3 and above on bare KB and VC compounds at larger overpotentials (Fig. 5f) due to  $\text{H}_2\text{O}_2$  reduction catalysed by narrow micropores ( $<0.7$  nm).<sup>48</sup> In rGO, the  $n$  value is almost constant throughout the applied potential due to the negligible number of narrow micropores (Section 3.1). The introduction of  $\text{Fe}_3\text{C}$  in the carbon materials exhibits improved  $E_{\text{onset}}$  and  $E_{1/2}$

and  $j_{\text{DL}}$ , indicating a positive impact of  $\text{Fe}_3\text{C}$  on the ORR activity. The positive shift in  $E_{\text{onset}}$  and  $E_{1/2}$  is more pronounced in  $\text{Fe}_3\text{C}/\text{NC}$  than in  $\text{Fe}_3\text{C}/\text{C}$ . The  $E_{\text{onset}}$  values are 0.96 ( $\text{Fe}_3\text{C}/\text{NKB}$ ), 0.90 ( $\text{Fe}_3\text{C}/\text{NVC}$ ) and 0.95 V ( $\text{Fe}_3\text{C}/\text{NrGO}$ ), which are 70, 50 and 30 mV more positive than those of  $\text{Fe}_3\text{C}/\text{KB}$ ,  $\text{Fe}_3\text{C}/\text{VC}$  and  $\text{Fe}_3\text{C}/\text{rGO}$ , respectively. Similarly,  $E_{1/2}$  values show a positive shift and the limiting current improved in  $\text{Fe}_3\text{C}/\text{NC}$  materials. Besides, a well-defined mass transport-controlled limiting region was observed with smaller ring currents. The  $n$  values are increased for  $\text{Fe}_3\text{C}/\text{NC}$  catalysts compared with  $\text{Fe}_3\text{C}/\text{C}$  catalysts (Fig. 5d and e). The  $n$  value of  $\text{Fe}_3\text{C}/\text{NKB}$  and  $\text{Fe}_3\text{C}/\text{NVC}$  compounds is 3.9, indicating the complete reduction of  $\text{O}_2$  to  $\text{H}_2\text{O}$ . The RRDE voltammograms of  $\text{Fe}_3\text{C}/\text{C}$ ,  $\text{Fe}_3\text{C}/\text{NC}$ , NC and only carbon supports at various rotational speeds are given in Fig. S11.†

Nitrogen-doped carbon materials were prepared without  $\text{Fe}_3\text{C}$  to study the role of  $\text{Fe}_3\text{C}$ . The ORR activity of N-doped carbon was evaluated under similar conditions. The comparison of the linear sweep voltammograms of  $\text{Fe}_3\text{C}/\text{C}$  and  $\text{Fe}_3\text{C}/\text{NC}$  with those of N–C catalysts is given in Fig. S11.† The comparison between the  $\text{Fe}_3\text{C}/\text{C}$  with N–C catalysts demonstrates that the N-doped carbon (N–C) catalysts (without  $\text{Fe}_3\text{C}$ ) show better  $E_{\text{onset}}$ ,  $E_{1/2}$  and  $j_{\text{DL}}$  values. The results indicate that  $\text{Fe}_3\text{C}$  is not the only reason for the improved ORR activity of  $\text{Fe}_3\text{C}/\text{NC}$ . The superior activity of  $\text{Fe}_3\text{C}/\text{NC}$  catalysts can be rationalized by the synergistic effect between the  $\text{Fe}_3\text{C}$  and N-doping active sites. Nevertheless, heating  $\text{Fe}_3\text{C}/\text{C}$  with nitrogen precursors can lead to formation of  $\text{Fe-N}_x$  species, popularly known as active sites

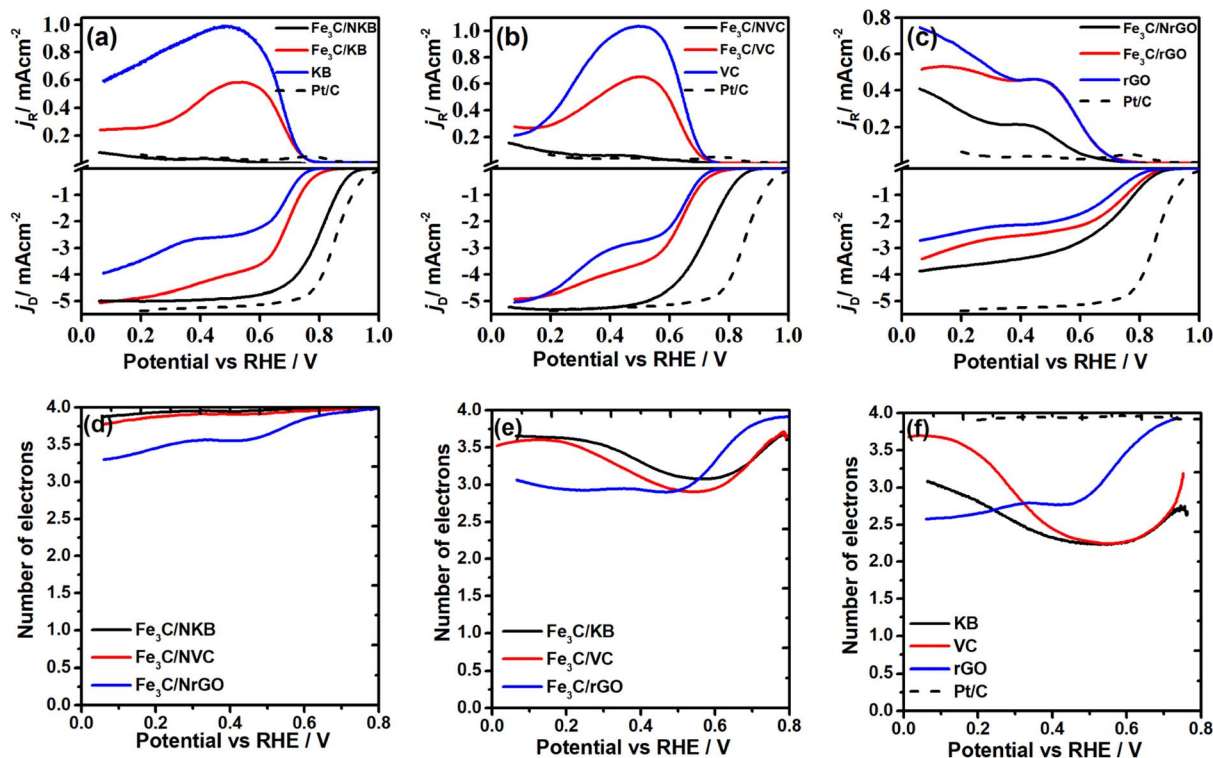


Fig. 5 RRDE voltammograms of the ORR on a pure carbon substrate, bare carbon support, and  $\text{Fe}_3\text{C}/\text{C}$  and  $\text{Fe}_3\text{C}/\text{NC}$  material (a–c) coated GC electrode in  $\text{O}_2$ -saturated 0.1 M KOH electrolyte at a scan rate of  $10 \text{ mV s}^{-1}$ . The dotted line represents the benchmark Pt/C catalysts (loading density  $20 \mu\text{g}_{\text{Pt}} \text{ cm}^{-2}$ ). The ring potential was kept at 1.2 V, and the electrode rotational speed was 1600 rpm. The number of electrons estimated from the ring and disk currents with applied potential on (d)  $\text{Fe}_3\text{C}/\text{NC}$ , (e)  $\text{Fe}_3\text{C}/\text{C}$  and (f) carbon supports with the benchmark Pt/C catalyst.



for the ORR. These Fe–N<sub>x</sub> active sites can form only on the surface of Fe<sub>3</sub>C particles in smaller quantities and are very difficult to analyse quantitatively by XPS. Detailed mechanistic studies may help define the active sites and role of Fe<sub>3</sub>C in the ORR activity. The ORR activity of Fe<sub>3</sub>C/NC catalysts is compared with that of the benchmark Pt/C catalysts, coated on the glassy carbon disk of the RRDE with a loading density of 20 μg<sub>Pt</sub> cm<sup>−2</sup>. The Pt/C catalysts show *E*<sub>onset</sub> and *E*<sub>1/2</sub> potentials of 0.99 and 0.86 V, respectively, which are 30 (in *E*<sub>onset</sub>) and 60 mV (in *E*<sub>1/2</sub>) more positive compared to those of the best performing Fe<sub>3</sub>C/NKB catalyst.

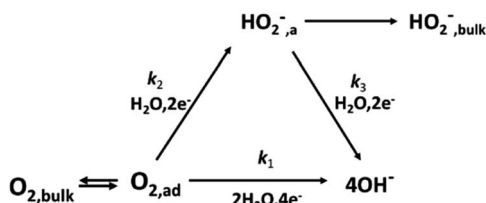
### 3.3 Kinetic & mechanistic analysis

The ORR mechanistic analysis shed some light on the various active sites responsible for the 2-electron and 4-electron ORR. The distinction between 2-electron and 4-electron active sites implies the critical roles of individual species in the catalysts. The elementary kinetic model proposed by Damjanovic *et al.*<sup>49</sup> can be used to calculate the rate constants, followed by the mechanistic analysis, as shown in Scheme 1.

The mass-balanced O<sub>2</sub> and HO<sub>2</sub><sup>−</sup> equations from the above kinetic model (Scheme 1) and disk and ring current equations are used to estimate the individual rate constants (see the ESI†).<sup>50,51</sup> The O<sub>2</sub> can be reduced to OH in a direct or indirect (peroxide) pathway. The direct reduction rate constant is referred to as *k*<sub>1</sub>, whereas *k*<sub>2</sub> (O<sub>2</sub> to HO<sub>2</sub><sup>−</sup>) and *k*<sub>3</sub> (HO<sub>2</sub><sup>−</sup> to OH<sup>−</sup>) indicate the peroxide pathway rate constants. The estimated

individual rate constants for Fe<sub>3</sub>C/C are shown in Fig. 6. Similarly, the rate constants of the bare carbon supports were estimated to study the role of Fe<sub>3</sub>C (Fig. S12†). The rate constant of O<sub>2</sub> to HO<sub>2</sub><sup>−</sup> (*k*<sub>2</sub>) is higher than *k*<sub>1</sub> (O<sub>2</sub> to OH<sup>−</sup>) on the carbon supports, indicating that the carbon supports facilitate the partial reduction of O<sub>2</sub>. However, Fe<sub>3</sub>C/C shows higher *k*<sub>1</sub> values indicating improved kinetics *via* the 4-electron pathway.<sup>52,53</sup> The increase in *k*<sub>1</sub> values is more significant in the lower applied potential region (<0.4 V for Fe<sub>3</sub>C/KB and Fe<sub>3</sub>C/VC), demonstrating the need for a higher overpotential for the complete 4-electron ORR. Fe<sub>3</sub>C/rGO does not show any improved 4-electron reduction activity at higher applied potentials, perhaps due to the nature of the carbon substrate. The *k*<sub>1</sub> value of Fe<sub>3</sub>C/C is 2–3 times higher than that of the bare carbon supports and it is more prominent for Fe<sub>3</sub>C/KB. This may be attributed to that KB could be a better host for the Fe<sub>3</sub>C particles due to its higher surface area and porous nature, which effectively retains Fe<sub>3</sub>C in pores. The carbon supports in Fe<sub>3</sub>C/C materials can catalyse the 2-electron ORR, indicated by smaller *k*<sub>2</sub> values. Based on the rate constants, the ORR activity can be arranged as Fe<sub>3</sub>C/KB > Fe<sub>3</sub>C/VC > Fe<sub>3</sub>C/rGO.

The presence of a heteroatom (N-doping) on the Fe<sub>3</sub>C/C composite (Fe<sub>3</sub>C/NC) brought about significant changes in the ORR kinetics. The estimated rate constants of Fe<sub>3</sub>C/NC compared to those of Fe<sub>3</sub>C/C are shown in Fig. 7. Fe<sub>3</sub>C/NKB exhibits the highest activity with a significant increase in the *k*<sub>1</sub> values even at more positive potential (lower overpotential region). Although Fe<sub>3</sub>C/NVC shows a similar trend as the Fe<sub>3</sub>C/NKB, the *k*<sub>2</sub> values are increasing with potential at the higher overpotential region. The notable increase in the *k*<sub>1</sub> values suggests that the heteroatom (nitrogen)-doping on Fe<sub>3</sub>C/C promotes the entire reduction reaction *via* the 4-electron pathway at lower overpotentials. Although Fe<sub>3</sub>C/NrGO shows a similar trend, the *k*<sub>1</sub> values are smaller than those of the other carbon supports. Conversely, the *k*<sub>2</sub> values of Fe<sub>3</sub>C/NC decrease at lower overpotentials (>0.4 V) compared with those of Fe<sub>3</sub>C/C, indicating a decrease in the 2-electron active sites. At higher overpotentials (<0.4 V), the *k*<sub>2</sub> value shows an increasing trend. The moderate increase in the 4-electron active sites from the



Scheme 1 Kinetic model of the oxygen reduction reaction proposed by Damjanovic *et al.* *k*<sub>1</sub>, *k*<sub>2</sub> and *k*<sub>3</sub> are the rate constants. 'ad' refers to the adsorbed species.

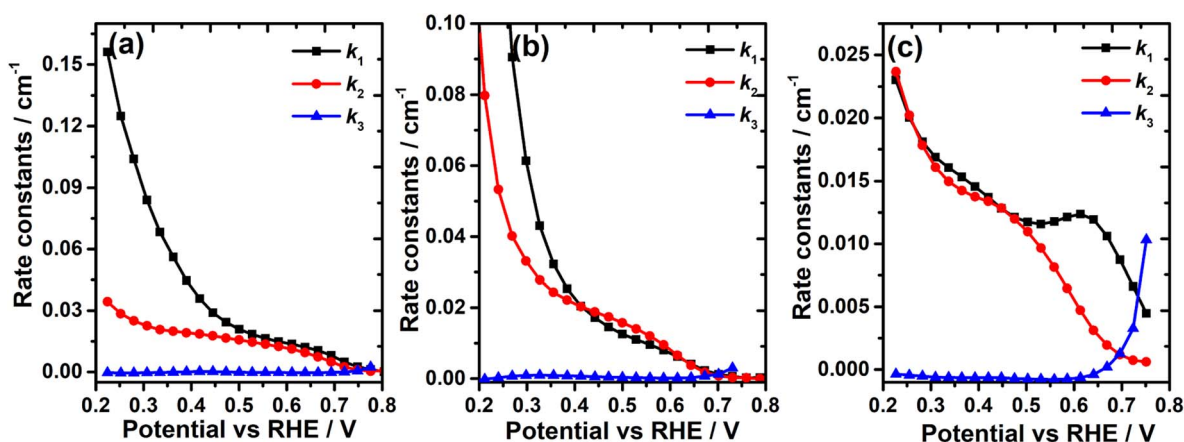


Fig. 6 Potential dependent rate constants of the ORR on (a) Fe<sub>3</sub>C/KB, (b) Fe<sub>3</sub>C/VC and (c) Fe<sub>3</sub>C/rGO composites.





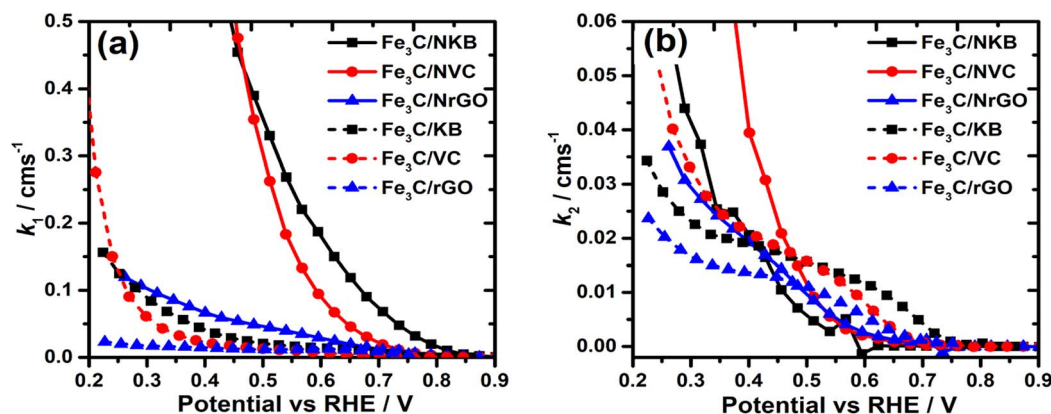


Fig. 7 Potential dependent rate constants (a)  $k_1$  and (b)  $k_2$  of the  $\text{Fe}_3\text{C}/\text{NC}$  (solid lines) and  $\text{Fe}_3\text{C}/\text{C}$  (dashed lines) catalysts.

bare carbon to  $\text{Fe}_3\text{C}/\text{C}$  and a significant improvement were observed while doping with nitrogen ( $\text{Fe}_3\text{C}/\text{NC}$ ), indicating the formation of 4-electron active sites from bare carbon to  $\text{Fe}_3\text{C}/\text{NC}$ .

The durability of the catalysts was examined using the accelerated durability test as explained in the Experimental section. The linear sweep rotating disk electrode voltammograms of the ORR on  $\text{Fe}_3\text{C}/\text{NC}$  catalysts before and after the 10 000 cycles of ADT are shown in Fig. 8. The  $E_{1/2}$  was taken to study the stability of the catalysts. The negative shift in the  $E_{1/2}$  values was observed in all three catalysts.  $\text{Fe}_3\text{C}/\text{NVC}$  shows high stability among the catalysts studied with a 30 mV negative shift, followed by  $\text{Fe}_3\text{C}/\text{NKB}$  (40 mV).  $\text{Fe}_3\text{C}/\text{NrGO}$  shows the least stability with a 120 mV negative shift. The  $j_{\text{DL}}$  shows a little decrease after the durability test for  $\text{Fe}_3\text{C}/\text{NKB}$  and  $\text{Fe}_3\text{C}/\text{NVC}$ . However, the decrease in the  $j_{\text{DL}}$  is significant in the case of  $\text{Fe}_3\text{C}/\text{NrGO}$ .

### 3.4 Zinc-air battery testing

A rechargeable zinc-air liquid electrolyte battery was assembled to evaluate the performance of  $\text{Fe}_3\text{C}/\text{NC}$  catalysts. Based on the previous reports,  $\text{Fe}_3\text{C}$  and N-C sites were assumed to be OER

and ORR active sites, respectively.<sup>19</sup> A Zn plate (0.5 mm thickness) and catalyst-coated carbon paper (with a loading density of  $1 \text{ mg cm}^{-2}$ ) were used as the anode and cathode, respectively. The electrodes were placed 1.5 cm apart, and the cell was filled with 6 M KOH + 0.2 M zinc acetate electrolyte.<sup>34</sup>

Discharge polarisation experiments were performed using chronopotentiometry (from zero to  $300 \text{ mA cm}^{-2}$ ), as shown in Fig. 9a. The highest positive open circuit potential (OCP) was observed ( $>1.5 \text{ V}$ ) for  $\text{Fe}_3\text{C}/\text{NC}$  (Fig. S13†).  $\text{Fe}_3\text{C}/\text{NVC}$  exhibits higher power density than the other two  $\text{Fe}_3\text{C}/\text{NC}$  materials, whereas  $\text{Fe}_3\text{C}/\text{NrGO}$  shows the lowest values among the three materials studied. The specific capacity of the  $\text{Fe}_3\text{C}/\text{NC}$  compounds was estimated from the chronopotentiometry experiment with a constant discharge current density of  $20 \text{ mA cm}^{-2}$  (Fig. 9b). The specific capacity varied from 650 to  $750 \text{ mA h g}_{\text{Zn}}^{-1}$ . The results obtained from the zinc-air battery testing are shown in Table 2. The charging-discharging profiles at various current densities are shown in Fig. 9c.

$\text{Fe}_3\text{C}/\text{NVC}$  shows excellent efficiency. The efficiency of the zinc-air battery was calculated from continuous galvanostatic charge-discharging (GCD) experiments (10 minutes of charging and 10 minutes of discharging with continuous 100 hours of

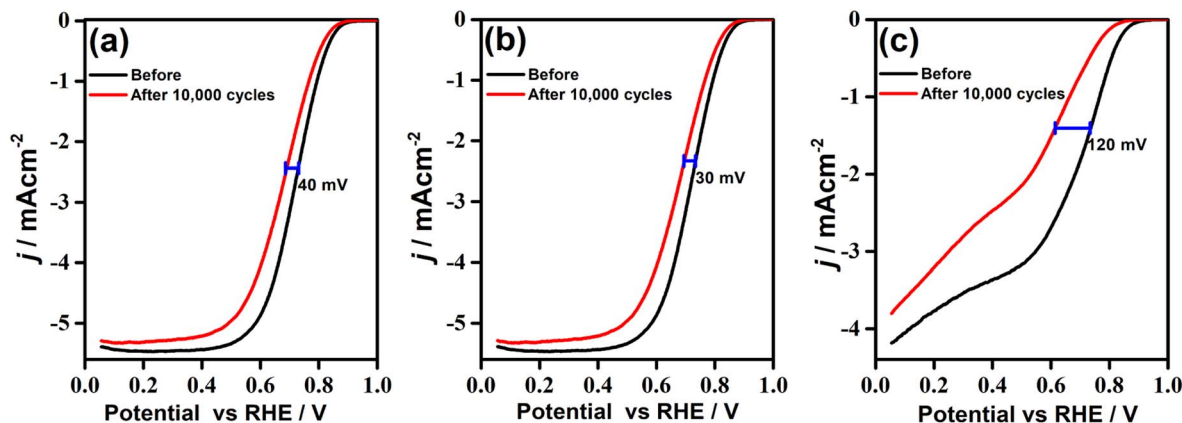


Fig. 8 The linear sweep voltammograms of the ORR on (a)  $\text{Fe}_3\text{C}/\text{NKB}$ , (b)  $\text{Fe}_3\text{C}/\text{NVC}$  and (c)  $\text{Fe}_3\text{C}/\text{NrGO}$  catalysts in  $\text{O}_2$ -saturated 0.1 M KOH electrolyte. The electrode rotational speed is 1600 rpm and the scan rate is  $10 \text{ mV s}^{-1}$ . The black and red lines indicate before and after the durability test.





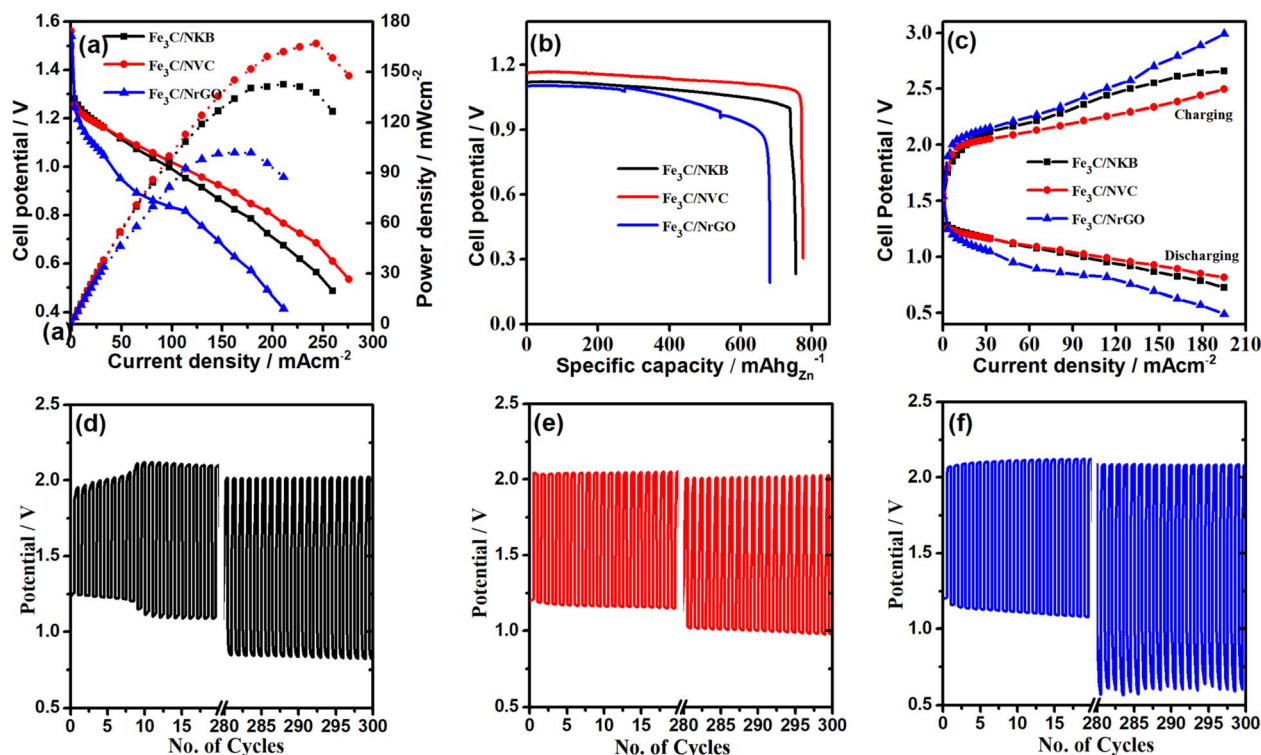


Fig. 9 (a) Discharge polarisation curves, (b) discharge profiles at a constant current of  $20 \text{ mA cm}^{-2}$  and (c) charging and discharging profiles of  $\text{Fe}_3\text{C}/\text{NC}$  materials. The galvanostatic charge–discharge cycles of (d)  $\text{Fe}_3\text{C}/\text{NKB}$ , (e)  $\text{Fe}_3\text{C}/\text{NVC}$  and (f)  $\text{Fe}_3\text{C}/\text{NrGO}$ . Only the initial and final 20 cycles are shown here.

operation) for 300 cycles with a current density of  $5 \text{ mA cm}^{-2}$ . The efficiency was calculated from the ratio of the potential window of the initial cycle (in the 10<sup>th</sup> cycle) to the final cycle (300<sup>th</sup> cycle). Fig. 9d–f show the first and last 20 charge–discharge cycles of the  $\text{Fe}_3\text{C}/\text{NC}$  catalysts.  $\text{Fe}_3\text{C}/\text{NVC}$  is found to be very stable for 300 cycles with an efficiency of 88%. This may be attributed to the lower Fe content (2.6 wt%) compared with the other materials (12 and 34 wt% in  $\text{Fe}_3\text{C}/\text{NKB}$  and  $\text{Fe}_3\text{C}/\text{NrGO}$ , respectively). Passivation and leaching could be possible reasons for deactivation of the catalytic activity in  $\text{Fe}_3\text{C}/\text{NKB}$  and  $\text{Fe}_3\text{C}/\text{NrGO}$  materials. The individual roles of  $\text{Fe}_3\text{C}$  and N-doped carbon/Fe–N can be evaluated based on the cycling performance, *i.e.*, GCD experiments.  $\text{Fe}_3\text{C}/\text{NC}$  materials show stable OER potential, and the charging potential did not increase even after 300 cycles. This can be rationalised from previous reports that  $\text{Fe}_3\text{C}$  sites facilitate the OER activity.

Conversely, the ORR overpotential increased (more than 200 mV) compared with the initial cycle (Fig. S16<sup>†</sup>), indicating that ORR activity decreases over a period of time. Therefore the bifunctional activity of  $\text{Fe}_3\text{C}/\text{NC}$  catalysts OER and ORR activity originates from  $\text{Fe}_3\text{C}$  and N–C/Fe–N, respectively.

To evaluate the bifunctional activity of  $\text{Fe}_3\text{C}/\text{NVC}$ , control experiments were carried out with the  $\text{Fe}_3\text{C}/\text{VC}$  and  $\text{NVC}$  catalysts. Both of them ( $\text{Fe}_3\text{C}/\text{VC}$  and  $\text{NVC}$ ) result in much lower power density and specific capacity values than  $\text{Fe}_3\text{C}/\text{NVC}$ . The GCD experiments indicate that the  $\text{Fe}_3\text{C}/\text{VC}$  catalysts are not stable for more than 230 cycles and the  $\text{NVC}$  catalysts are stable until 300 cycles. Despite its stability, the  $\text{NVC}$  catalyst showed lower efficiency than the  $\text{Fe}_3\text{C}/\text{NVC}$  catalyst. The benchmark ORR and OER catalysts were used to study the comparative performance of the zinc–air battery. Pt/C and Ir/C (1 : 1) were mixed to prepare the catalytic ink and coated under the similar conditions

Table 2 Zinc–air battery performance parameters of various  $\text{Fe}_3\text{C}/\text{NC}$  materials

Compounds	OCP (V)	Power density ( $\text{mW cm}^{-2}$ )	Current density <sup>a</sup> ( $\text{mA cm}^{-2}$ )	Specific capacity <sup>b</sup> ( $\text{mA h g}_{\text{Zn}}^{-1}$ )	Efficiency <sup>c</sup>
$\text{Fe}_3\text{C}/\text{NKB}$	1.50	142	211	738	79%
$\text{Fe}_3\text{C}/\text{NVC}$	1.56	167	243	756	88%
$\text{Fe}_3\text{C}/\text{NrGO}$	1.54	102	179	663	58%
Pt/C + Ir/C	1.44	154	244	729	62%

<sup>a</sup> Current density at a maximum power density. <sup>b</sup> Specific capacity is estimated with a constant discharge current of  $20 \text{ mA cm}^{-2}$ . <sup>c</sup> The efficiency was calculated from the 10<sup>th</sup> cycle to the 300<sup>th</sup> cycle (after 100 hours of continuous charging and discharging) difference with a charging and discharging current of  $5 \text{ mA cm}^{-2}$  where 10 minutes for charging and 10 minutes are for discharging.



described earlier. The power density value is  $154 \text{ mW cm}^{-2}$  less than that of the  $\text{Fe}_3\text{C}/\text{NVC}$  catalyst. The specific capacity and the GCD experiments indicate that  $\text{Fe}_3\text{C}/\text{NVC}$  and  $\text{Fe}_3\text{C}/\text{NKB}$  catalysts perform much better than benchmark catalysts. After the GCD cycles, the benchmark catalysts show poor performance in OER and ORR regions, indicating the superior bifunctional activity of  $\text{Fe}_3\text{C}/\text{NVC}$ . The performance of the  $\text{Pt}/\text{C} + \text{RuO}_2$  (1 : 1) catalysts was also used to compare the literature values. The discharge polarisation curves, specific capacity, and stability tests are given in the ESI (Fig. S13 to S17†).

### 3.5 Discussion

The N-doping on the  $\text{Fe}_3\text{C}/\text{C}$  composites led to improved ORR and OER activity. From the RRDE voltammograms and kinetic analysis, it was found that  $\text{Fe}_3\text{C}$  facilitates the ORR activity *via* the 4-electron pathway. Similarly, the nitrogen-doped carbon (NC) materials exhibit higher ORR activity than both bare carbon and  $\text{Fe}_3\text{C}/\text{C}$  materials. Hence the superior ORR activity of  $\text{Fe}_3\text{C}/\text{NC}$  catalysts can be defined by the synergy between  $\text{Fe}_3\text{C}/\text{C}$  and nitrogen-doped carbon sites.<sup>23,30</sup> The mechanism of the synergistic effect is not yet understood and it can be visualised either by the simultaneous involvement of the two active sites during the adsorption step or the involvement of individual active sites at different parts of the reactions to facilitate and sometimes both.<sup>55</sup> However, the possibility of the formation of  $\text{Fe}-\text{N}_x$  active sites on the surface of  $\text{Fe}_3\text{C}$  particles during the pyrolysis of  $\text{Fe}_3\text{C}$  with nitrogen precursors cannot be eliminated. The kinetic analysis indicates that a significant increase in the direct 4-electron reduction rate constant ( $k_1$ ) of the ORR on  $\text{Fe}_3\text{C}/\text{NC}$  supports the formation of  $\text{Fe}-\text{N}_x$ . XPS cannot detect the  $\text{Fe}-\text{N}$  sites, perhaps due to the smaller content. Furthermore, the ORR activity of the physical mixture of the  $\text{Fe}_3\text{C}/\text{C}$  and NC materials was analysed to evaluate the synergistic effect and the importance of  $\text{Fe}-\text{N}_x$  active sites. The physical mixture of  $\text{Fe}_3\text{C}/\text{C}$  and NC compounds does not contain any  $\text{Fe}-\text{N}_x$  active sites but consists of  $\text{Fe}_3\text{C}$  and  $\text{N}-\text{C}$  active sites. The ORR activity of such physical mixture catalysts exhibits less ORR activity than individual catalysts such as  $\text{Fe}_3\text{C}/\text{C}$ , NC and  $\text{Fe}_3\text{C}/\text{NC}$ . This indicates the role of  $\text{Fe}-\text{N}_x$  in the ORR activity. On the other side, the  $\text{Fe}_3\text{C}$  active sites contribute to the OER activity.<sup>19,37,56</sup> The OER potential did not increase even after 300 charge–discharge cycles (100 hours), indicating that the materials are very stable for the OER irrespective of the supporting carbon materials.  $\text{Fe}_3\text{C}$  active sites could be the OER active sites, irrespective of the type of carbon support and nitrogen content. Nevertheless, the role of  $\text{Fe}-\text{N}_x$  in the OER cannot be neglected. The higher stability of  $\text{Fe}_3\text{C}/\text{NVC}$  catalysts can be seen from the lower Fe content (2 wt%). Higher Fe content materials are susceptible to passivation and leaching, deactivating the catalytic activity. Finally, the ORR and OER are catalysed by  $\text{Fe}-\text{N}_x$  and  $\text{Fe}_3\text{C}$  sites, respectively.

## 4. Conclusions

The role of  $\text{Fe}_3\text{C}$  in  $\text{Fe}_3\text{C}$  incorporated nitrogen-doped carbon materials was studied on various carbon supports of different

porosities. The PB-carbon (KB, VC, and rGO) composites were pyrolysed in an inert atmosphere, leading to  $\text{Fe}_3\text{C}/\text{C}$ . The following conclusions were drawn after the series of half-cell, kinetic analysis and zinc–air battery experiments to define the role of  $\text{Fe}_3\text{C}$ .

$\text{Fe}_3\text{C}/\text{C}$  shows improved ORR activity compared with the bare carbon supports. Besides the positive shift in  $E_{\text{onset}}$  and  $E_{1/2}$  values, the kinetics analysis demonstrates the increasing rate constants of direct 4-electron reduction. This implies the generation of 4-electron active sites due to the introduction of  $\text{Fe}_3\text{C}$  on carbon supports.

The heteroatom (nitrogen)-doping on  $\text{Fe}_3\text{C}/\text{C}$  exhibits superior activity, which may be attributed to the synergistic effect of  $\text{Fe}_3\text{C}$  and  $\text{N}-\text{C}$  active sites or  $\text{Fe}-\text{N}_x$  sites. The kinetic analysis demonstrates that the direct 4-electron reduction rate constants increased even at more positive potentials, supporting the formation of  $\text{Fe}-\text{N}_x$  active sites.

The zinc–air battery shows excellent performance while using  $\text{Fe}_3\text{C}/\text{NVC}$  as the OER and ORR catalyst. The highest positive OCP (1.56 V) and specific capacity ( $756 \text{ mA h g}_{\text{Zn}}^{-1}$ ) with a power density of  $167 \text{ mW cm}^{-2}$  were obtained, which is higher than that of the benchmark catalyst  $\text{Pt}/\text{C} + \text{Ir}/\text{C}$  (1 : 1). Besides,  $\text{Fe}_3\text{C}/\text{NVC}$  shows an excellent efficiency (88%).

Finally, the  $\text{Fe}_3\text{C}$  and  $\text{N}-\text{C}$  combination and/or  $\text{Fe}-\text{N}_x$  active sites could be responsible for the ORR activity.  $\text{Fe}_3\text{C}/\text{NVC}$  consists of lower Fe content that shows higher stability. The  $\text{Fe}_3\text{C}$  active sites are facilitating the OER. Hence the materials consisting of  $\text{Fe}_3\text{C}$ ,  $\text{N}-\text{C}$  and  $\text{Fe}-\text{N}_x$  act as excellent bifunctional catalysts for rechargeable zinc–air batteries.

## Author contributions

S. A. G. performed the synthesis, characterisation of materials and electrochemical experiments. A. N. E. performed all zinc–air battery experiments. A. M. designed, supervised and wrote the manuscript.

## Conflicts of interest

There are no conflicts to declare.

## Acknowledgements

SA thanks CSIR (UGC), India for a fellowship. We thank IISER for the facilities. The authors thank LION Specialty Chemical Co., Ltd., for the carbon samples. Also, the authors thank the reviewers for their enlightening comments on revising the manuscript.

## Notes and references

- X. Hu, S. Chen, L. Chen, Y. Tian, S. Yao, Z. Lu, X. Zhang and Z. Zhou, *J. Am. Chem. Soc.*, 2022, **144**, 18144–18152.
- Y. Jia, L. Zhang, L. Zhuang, H. Liu, X. Yan, X. Wang, J. Liu, J. Wang, Y. Zheng, Z. Xiao, E. Taran, J. Chen, D. Yang, Z. Zhu, S. Wang, L. Dai and X. Yao, *Nat. Catal.*, 2019, **2**, 688–695.



- 3 Y. Chen, I. Matanovic, E. Weiler, P. Atanassov and K. Artyushkova, *ACS Appl. Energy Mater.*, 2018, **1**, 5948–5953.
- 4 K. Artyushkova, A. Serov, S. Rojas-Carbonell and P. Atanassov, *J. Phys. Chem. C*, 2015, **119**, 25917–25928.
- 5 U. Tylus, Q. Jia, K. Strickland, N. Ramaswamy, A. Serov, P. Atanassov and S. Mukerjee, *J. Phys. Chem. C*, 2014, **118**, 8999–9008.
- 6 W. Li, J. Wu, D. C. Higgins, J.-Y. Choi and Z. Chen, *ACS Catal.*, 2012, **2**, 2761–2768.
- 7 C. V. Rao, C. R. Cabrera and Y. Ishikawa, *J. Phys. Chem. Lett.*, 2010, **1**, 2622–2627.
- 8 T. Ikeda, M. Boero, S.-F. Huang, K. Terakura, M. Oshima and J.-i. Ozaki, *J. Phys. Chem. C*, 2008, **112**, 14706–14709.
- 9 M. Lefevre, J. P. Dodelet and P. Bertrand, *J. Phys. Chem. B*, 2002, **106**, 8705–8713.
- 10 C.-X. Zhao, D. Ren, J. Wang, J.-N. Liu, C. Tang, X. Chen, B.-Q. Li and Q. Zhang, *J. Energy Chem.*, 2022, **73**, 478–484.
- 11 L. Peng, J. Yang, Y. Yang, F. Qian, Q. Wang, D. Sun-Waterhouse, L. Shang, T. Zhang and G. I. N. Waterhouse, *Adv. Mater.*, 2022, **34**, 2202544.
- 12 X. Xie, L. Shang, X. Xiong, R. Shi and T. Zhang, *Adv. Energy Mater.*, 2022, **12**, 2102688.
- 13 Y. Wang, L. Wang, Y. Xie, M. M. Tong, C. G. Tian and H. G. Fu, *ACS Sustainable Chem. Eng.*, 2022, **10**, 3346–3354.
- 14 Z. X. Cao, J. Y. Jia, H. H. Li, Y. H. Wang, X. X. Mao, Z. N. Zhang, M. G. Yang and S. T. Yang, *Int. J. Hydrogen Energy*, 2020, **45**, 3930–3939.
- 15 X. X. Yang, X. L. Hu, X. L. Wang, W. Fu, X. Q. He and T. Asefa, *J. Electroanal. Chem.*, 2018, **823**, 755–764.
- 16 Y. L. Niu, X. Q. Huang and W. H. Hu, *J. Power Sources*, 2016, **332**, 305–311.
- 17 G. K. Wang, W. L. Wang, Y. Chen, C. L. Yan and Z. Y. Gao, *Appl. Surf. Sci.*, 2023, **610**, 155456.
- 18 Z. Y. Han, W. F. Cai, S. F. Zhao, Y. Zhao, J. R. Bai, Q. Y. Chen and Y. H. Wang, *Nanoscale*, 2022, **14**, 18157–18166.
- 19 M. Cao, Y. Liu, K. Sun, H. Li, X. Lin, P. Zhang, L. Zhou, A. Wang, S. Mehdi, X. Wu, J. Jiang and B. Li, *Small*, 2022, **18**, 2202014.
- 20 B. H. Zhang, J. Chen, H. H. Guo, M. Y. Le, H. Z. Guo, Z. Y. Li and L. Wang, *ACS Appl. Nano Mater.*, 2021, **4**, 8360–8367.
- 21 S. A. Abbas, D. Seo, H. Jung, Y. J. Lim, A. Mehmood and K. M. Nam, *Appl. Surf. Sci.*, 2021, **551**, 149445.
- 22 W. X. She, Q. R. Xie, Y. H. Huang, C. Y. Xie, X. Y. Zhang, M. C. Sun, F. Wang and J. W. Xiao, *ACS Appl. Mater. Interfaces*, 2020, **12**, 28065–28074.
- 23 L. L. Cui, Q. L. Zhang and X. Q. He, *J. Electroanal. Chem.*, 2020, **871**, 114316.
- 24 Z. Y. Wu, X. X. Xu, B. C. Hu, H. W. Liang, Y. Lin, L. F. Chen and S. H. Yu, *Angew. Chem., Int. Ed.*, 2015, **54**, 8179–8183.
- 25 H. L. Jiang, Y. F. Yao, Y. H. Zhu, Y. Y. Liu, Y. H. Su, X. L. Yang and C. Z. Li, *ACS Appl. Mater. Interfaces*, 2015, **7**, 21511–21520.
- 26 H. Xu, C. Zhang, Z. Wang, S. Pang, X. Zhou, Z. Zhang and G. Cui, *J. Mater. Chem. A*, 2014, **2**, 4676–4681.
- 27 Z. Chen, X. M. Gao, X. R. Wei, X. X. Wang, Y. G. Li, T. Wu, J. Guo, Q. F. Gu, W. D. Wu, X. D. Chen, Z. X. Wu and D. Y. Zhao, *Carbon*, 2017, **121**, 143–153.
- 28 Y. Hu, J. O. Jensen, W. Zhang, L. N. Cleemann, W. Xing, N. J. Bjerrum and Q. F. Li, *Angew. Chem., Int. Ed.*, 2014, **53**, 3675–3679.
- 29 W. J. Jiang, L. Gu, L. Li, Y. Zhang, X. Zhang, L. J. Zhang, J. Q. Wang, J. S. Hu, Z. D. Wei and L. J. Wan, *J. Am. Chem. Soc.*, 2016, **138**, 3570–3578.
- 30 X. H. Yan, P. Prabhu, H. Xu, Z. Meng, T. Xue and J. M. Lee, *Small Methods*, 2019, **4**, 1900575.
- 31 X. R. Zhang, D. D. Lyu, Y. B. Mollamahale, F. Yu, M. Qing, S. B. Yin, X. Y. Zhang, Z. Q. Tian and P. K. Shen, *Electrochim. Acta*, 2018, **281**, 502–509.
- 32 Y. Zhang, W. J. Jiang, L. Guo, X. Zhang, J. S. Hu, Z. D. Wei and L. J. Wan, *ACS Appl. Mater. Interfaces*, 2015, **7**, 11508–11515.
- 33 G. Y. Zhong, H. J. Wang, H. Yu and F. Peng, *J. Power Sources*, 2015, **286**, 495–503.
- 34 J. H. Kim, Y. J. Sa, H. Y. Jeong and S. H. Joo, *ACS Appl. Mater. Interfaces*, 2017, **9**, 9567–9575.
- 35 R. Venegas, C. Zuniga, J. H. Zagal, A. Toro-Labbe, J. F. Marco, N. Menendez, K. Munoz-Becerra and F. J. Recio, *ChemElectroChem*, 2022, **9**, 20220011.
- 36 B. K. Barman and K. K. Nanda, *Green Chem.*, 2016, **18**, 427–432.
- 37 Z. Peng, H. T. Wang, X. C. Xia, X. X. Zhang and Z. H. Dong, *ACS Sustainable Chem. Eng.*, 2020, **8**, 9009–9016.
- 38 Y. Y. Qiao, P. F. Yuan, Y. F. Hu, J. N. Zhang, S. C. Mu, J. H. Zhou, H. Li, H. C. Xia, J. He and Q. Xu, *Adv. Mater.*, 2018, **30**, 1804504.
- 39 W. S. Hummers and R. E. Offeman, *J. Am. Chem. Soc.*, 1958, **80**, 1339.
- 40 A. N. Eledath, A. E. Poullose and A. Muthukrishnan, *ACS Appl. Nano Mater.*, 2022, **5**, 10528–10536.
- 41 J. Anjana and A. Muthukrishnan, *Catal. Sci. Technol.*, 2022, **12**, 6246–6255.
- 42 P. Rao, J. Luo, J. Li, W. Huang, W. Sun, Q. Chen, C. Jia, Z. Liu, P. Deng, Y. Shen and X. Tian, *Carbon Energy*, 2022, **4**, 1003–1010.
- 43 S. Arya Gopal, A. Edathiparambil Poullose, C. Sudakar and A. Muthukrishnan, *ACS Appl. Mater. Interfaces*, 2021, **13**, 44195–44206.
- 44 G. Liu, X. Li, P. Ganesan and B. N. Popov, *Electrochim. Acta*, 2010, **55**, 2853–2858.
- 45 Q. Lv, W. Si, J. He, L. Sun, C. Zhang, N. Wang, Z. Yang, X. Li, X. Wang, W. Deng, Y. Long, C. Huang and Y. Li, *Nat. Commun.*, 2018, **9**, 3376.
- 46 T. Soboleva, X. Zhao, K. Malek, Z. Xie, T. Navessin and S. Holdcroft, *ACS Appl. Mater. Interfaces*, 2010, **2**, 375–384.
- 47 H. B. Tan, Y. Q. Li, J. Kim, T. Takei, Z. L. Wang, X. T. Xu, J. Wang, Y. Bando, Y. M. Kang, J. Tang and Y. Yamauchi, *Adv. Sci.*, 2018, **5**, 1800120.
- 48 A. Gabe, R. Ruiz-Rosas, C. González-Gaitán, E. Morallón and D. Cazorla-Amorós, *J. Power Sources*, 2019, **412**, 451–464.
- 49 A. Damjanovic, M. A. Genshaw and J. O. M. Bockris, *J. Chem. Phys.*, 1966, **45**, 4057–4059.
- 50 K. L. Hsueh, D. T. Chin and S. Srinivasan, *J. Electroanal. Chem.*, 1983, **153**, 79–95.





- 51 A. Muthukrishnan, Y. Nabaie, T. Hayakawa, T. Okajima and T. Ohsaka, *Catal. Sci. Technol.*, 2015, **5**, 475–483.
- 52 A. Muthukrishnan and Y. Nabaie, *J. Phys. Chem. C*, 2016, **120**, 22515–22525.
- 53 A. Muthukrishnan, Y. Nabaie, T. Okajima and T. Ohsaka, *ACS Catal.*, 2015, **5**, 5194–5202.
- 54 C.-X. Zhao, J.-N. Liu, B.-Q. Li, D. Ren, X. Chen, J. Yu and Q. Zhang, *Adv. Funct. Mater.*, 2020, **30**, 2003619.
- 55 E. A. A. Nazer and A. Muthukrishnan, *Catal. Sci. Technol.*, 2020, **10**, 6659–6668.
- 56 C. Lin, X. Li, S. S. Shinde, D.-H. Kim, X. Song, H. Zhang and J.-H. Lee, *ACS Appl. Energy Mater.*, 2019, **2**, 1747–1755.

